



The effect of 24c-site (A) cation substitution on the tetragonal–cubic phase transition in $\text{Li}_{7-x}\text{La}_{3-x}\text{A}_x\text{Zr}_2\text{O}_{12}$ garnet-based ceramic electrolyte

Ezhilmurugan Rangasamy ^a, Jeff Wolfenstine ^b, Jan Allen ^a, Jeff Sakamoto ^{a,*}

^a Department of Chemical Engineering and Materials Science, Michigan State University, East Lansing, MI 48824, USA

^b Army Research Laboratory, RDRL-SED-C, 2800 Powder Mill Road, Adelphi, MD 20783, USA

HIGHLIGHTS

- Substitution of La with Ce stabilizes the cubic LLZO garnet phase.
- CeO_2 precipitation at grain boundaries increases grain boundary resistance.
- Super-valent cation substitution likely stabilizes the cubic LLZO phase.

ARTICLE INFO

Article history:

Received 15 July 2012

Received in revised form

16 November 2012

Accepted 6 December 2012

Available online 27 December 2012

Keywords:

Solid-electrolyte

Garnet

Ce

Cubic

Li vacancies

Hot-pressing

ABSTRACT

The garnet-type ceramic electrolyte of nominal composition $\text{Li}_7\text{La}_3\text{Zr}_2\text{O}_{12}$ can exist in the tetragonal and cubic form. This article investigates the tetragonal to cubic phase transition based on super-valent cation substitution on the 24c site typically occupied by La (3+) in the garnet structure. Ce (4+) was selected as the super-valent cation represented as x in $\text{Li}_{7-x}\text{La}_{3-x}\text{Ce}_x\text{Zr}_2\text{O}_{12}$. The doping study showed that cubic LLZO was stabilized for $\text{Ce} \geq 0.2$. These data agree with most literature reports suggesting that the creation of Li vacancies, while maintaining oxygen stoichiometry, is necessary to stabilize cubic LLZO. Moreover, this work suggests a critical Li vacancy concentration (0.12–0.4 mol per mole of $\text{Li}_7\text{La}_3\text{Zr}_2\text{O}_{12}$) is necessary to stabilize cubic LLZO. While the addition of Ce stabilized cubic LLZO, the total ionic conductivity (0.014 mS cm^{-1}) was considerably lower compared to Al and Ta doped LLZO (0.4 – 0.9 mS cm^{-1} , respectively). The lower conductivity is likely due to CeO_2 precipitation at grain boundaries.

© 2012 Elsevier B.V. All rights reserved.

1. Introduction

Li-ion batteries have played a vital role in the development of current generation mobile devices, microelectronics and electric vehicles [1]. Due to the flammability of conventional electrolytes [2], considerable research has been conducted to develop solid state Li-ion conductors [3–5]. Ceramic Li ion conductors have high thermal, chemical and electrochemical stability vs. Li/Li⁺ [4], which could enable the use of ultrahigh voltage cathodes. The unique combination of high ionic conductivity, chemical and electrochemical stability could also enable the development of Li-air, redox flow and Li–S secondary batteries.

A number of solid state Li-ion conductors demonstrate potential for use in advanced battery technology [3–5]. Of these, the most

common has been the family of perovskite titanates ($\text{Li}_{3x}\text{La}_{2/3-x}\text{TiO}_3$) (LLTO) and NASICON type $\text{Li}_{1.3}\text{Al}_{0.3}\text{Ti}_{1.7}(\text{PO}_4)_3$ (LATP) [3–7]. Despite having a high bulk Li-ion conductivity of 1 mS cm^{-1} , polycrystalline LLTO typically has low grain boundary conductivity, thus reducing the total conductivity to the 10^{-5} to $10^{-6} \text{ S cm}^{-1}$ range [5–7]. Additionally, the presence of Ti limits the voltage stability vs. Li/Li⁺ to approximately 1.7 V in the perovskite LLTO and 2.5 V in LATP [8,9], thus preventing use with metallic Li or other low potential anodes. $\text{Li}_7\text{La}_3\text{Zr}_2\text{O}_{12}$ (LLZO) with the garnet structure is a promising ceramic electrolyte, because it exhibits the unprecedented combination of high room temperature total conductivity of $0.9 \times 10^{-3} \text{ S cm}^{-1}$ [10] and electrochemical stability against metallic lithium [11,12].

It has been reported that tetragonal LLZO has a Li-ion conductivity that is approximately between two and three orders of magnitude lower than the cubic LLZO [13–16]. Thus, the challenge has been to stabilize the cubic form of LLZO. The first reported stabilization of the cubic LLZO resulted from the adventitious

* Corresponding author. Tel.: +1 517 432 7393; fax: +1 517 432 1105.

E-mail address: jsakomat@msu.edu (J. Sakamoto).

doping of Al as a result of contamination from alumina crucibles [10,17]. Later Al was intentionally added [18,19] and a dense (relative density > 90%) material with a cubic structure was obtained. Geiger et al. [17] have suggested that Al substitutes for Li and thereby stabilizes the cubic phase. A similar stabilization of cubic phase is observed with Ga substitution, where Ga substitutes for Li [20,21]. One hypothesis is that super-valent cation substitution reduces the Li content and/or increases Li vacancy concentration, while maintaining oxygen stoichiometry, and hence stabilizes the cubic phase [16,17,19]. In Kroger–Vink notation [24], the relationship for Al and Ga substitution for Li are as follows [17,19,21]:

$$2[\text{Al}_{\text{Li}}] = [\text{V}'_{\text{Li}}] \quad (1)$$

$$2[\text{Ga}_{\text{Li}}] = [\text{V}'_{\text{Li}}] \quad (2)$$

However, substitutions for Li^+ (as is the case for Al and Ga) result in the obstruction of ionic pathways, thus reducing the conductivity [20]. Another super-valent substitution scheme involves either Nb (5+) or Ta (5+) on the 16a site (Zr 4+), that reduces the Li content and/or increases Li vacancy concentration to stabilize the cubic structure [22,23]. Substitution on the Zr (4+) site will not block the Li-ion pathways and thus leads to higher conductivity than that observed for the Al and Ga substitutions [20]. For example, when 0.25 mol of Ta was substituted for 0.25 mol of Zr, the conductivity more than doubled compared to comparable levels of doping with Al [16,20]. In Kroger–Vink notation, the relationships for Ta and Nb substitution for Zr are as follows [20,22,23]:

$$[\text{Ta}_{\text{Zr}}] = [\text{V}'_{\text{Li}}] \quad (3)$$

$$[\text{Nb}_{\text{Zr}}] = [\text{V}'_{\text{Li}}] \quad (4)$$

Likewise, super-valent substitution on the 24c (La 3+) is another approach to create Li vacancies without obstructing the Li sub-lattice, that could stabilize the cubic LLZO phase. At present there is no information regarding the stabilization of cubic LLZO by the substitution of super-valent cation (4+) on the La (3+).

It follows that the purpose of this work is to investigate the tetragonal to cubic phase transition based on super-valent substitution of Ce (4+) for La (3+) in the formula $\text{Li}_{7-x}\text{La}_{3-x}\text{Ce}_x\text{Zr}_2\text{O}_{12}$. In Kroger–Vink notation, the proposed substitution would be:

$$[\text{Ce}_{\text{La}}] = [\text{V}'_{\text{Li}}] \quad (5)$$

In 8-fold coordination, the radius of Ce (4+) (128 pm) is similar to La (3+) (130 pm), thus substitution is expected [24]. The proposed range of x is $0.0 < x < 0.8$ and is based on similar work involving Al, Ga, Nb and Ta where the Al was intentionally added [18–23].

In this work, a series of Ce doped LLZO powder samples were prepared using a conventional solid state reaction technique. Measures were taken to eliminate Al contamination from alumina crucibles as a variable has been reported previously [19]. The powders were characterized using X-ray diffraction (XRD) to determine the phase(s) present, followed by densification to >94% relative density to evaluate the ionic transport of selected formulations. SEM analysis was used to characterize the microstructures and phase impurities. Additionally, the ionic transport was characterized using electrochemical impedance spectroscopy and the activation energies were measured between 298 and 378 K.

2. Experimental

2.1. Synthesis

Lithium carbonate (Alfa Aesar 99.998%), lanthanum hydroxide (Alfa Aesar 99.95%), zirconium oxide (30–60 nm 99.9% Inframal Advanced Materials), and cerium oxide (50–80 nm 99.97% Inframal Advanced Materials) powders were used as precursor materials during the synthesis procedure. The precursor powders were weighed according to the formula $\text{Li}_{7-x}\text{La}_{3-x}\text{Ce}_x\text{Zr}_2\text{O}_{12}$ where $x = 0.0, 0.2, 0.4, 0.6$ and 0.8 mol. (no excess Li precursor was added). The precursors were milled in a planetary mill for 4 h (Planetary Mill PM 100 – Retsch) using agate media, cold pressed and calcined at 1000 °C for 4 h in air in a tube furnace (Thermo Scientific Lindberg Blue M Mini-Mite). To prevent Al contamination, powders were calcined on pristine zirconia surfaces. Powders were placed in graphite dies and hot pressed at 1050 °C under flowing argon for 1 h under 40 MPa pressure.

2.2. Characterization

Specimen densities were calculated using geometric and gravimetric measurements. Identification of crystal phases was carried out using XRD (Bruker D8 Advance with Da Vinci) and microstructure analysis was carried out using SEM (JEOL JSM 7500F). Grain sizes were established using a linear intercept method on the SEM micrographs. Energy Dispersive Spectroscopy (EDS) analysis was carried out in a Carl Zeiss variable pressure SEM (EVO LS25). Elemental analysis carried out using EDS utilized five line scans per sample with a resolution of 0.1 μm on the line scan, with each line being averaged over 6 scans. Samples for EDS analysis were mounted in a conductive epoxy and mechanically polished to a final finish using a 50 nm Al_2O_3 – water slurry. Volume fraction of ceria was calculated using the histographic analysis of Back Scattered Electron (BSE) imaged samples. Li ion conductivity was determined using AC electrochemical impedance spectroscopy (EIS) with a VersaSTAT4 potentiostat over a frequency range of 10 Hz–800 kHz and potential amplitude of 100 mV. For electrochemical measurements, the sintered pellets were coated with Au films of an approximate thickness of 105 nm using sputter coating. A load frame applied a constant 0.34 MPa pressure during EIS measurements.

3. Results and discussion

3.1. Effect of Ce on the crystal structure of LLZO

The X-ray diffraction (XRD) patterns for the range of $0.0 < x < 0.8$ Ce in the formula $\text{Li}_{7-x}\text{La}_{3-x}\text{Ce}_x\text{Zr}_2\text{O}_{12}$ are shown in Fig. 1. When $x = 0.0$ Ce, tetragonal LLZO forms as is evident from peak doublets associated with primary peaks, which is in agreement with previous work [13–16]. In previous work [19] the peak at $2\theta = 34^\circ$ was used to identify peak doublets. However, in this work, a high intensity peak, from the secondary phase CeO_2 at $2\theta = 34^\circ$, obscured the tetragonal peak doublets at $2\theta = 34^\circ$. Thus, the 50 – 55° 2θ range was used to determine if the cubic or tetragonal LLZO phase was present. If LLZO is cubic, there are three peaks and if LLZO is tetragonal there are six peaks in the 50 – 55° 2θ range. A box highlights these peaks in Fig. 1.

When x is increased (Ce added), several observations can be made. First, it is clear that the addition of Ce stabilizes the cubic LLZO phase. The peak doublet intensities decrease as x increases, indicating that the addition of Ce is what drives the transformation from tetragonal to cubic LLZO. The peak doublet intensities significantly decrease between $x = 0.2$ Ce and $x = 0.4$ Ce diminishing to

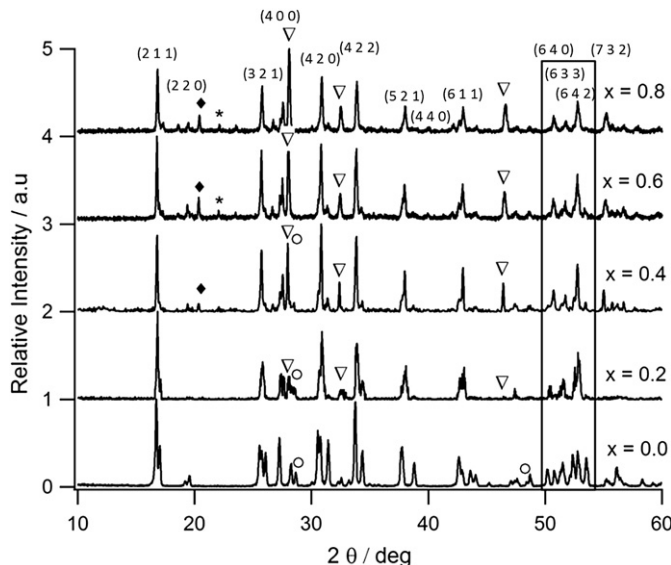


Fig. 1. XRD data for $0.0 < x < 0.8$ in $\text{Li}_{7-x}\text{La}_{3-x}\text{Ce}_x\text{Zr}_2\text{O}_{12}$. ∇ indicates the presence of CeO_2 , \circ indicates the presence of $\text{La}_2\text{Zr}_2\text{O}_7$, \blacklozenge indicates the presence of Li_2ZrO_3 and $*$ indicates the presence of an unknown phase. The box highlights the group of peaks used to determine if the cubic or tetragonal phase was present. The lattice planes of the garnet have been indexed according to the JCPDS 45-109.

nearly undetectable values when $x = 0.8$ Ce. Secondly, the relative CeO_2 peak intensities increased from $x = 0.4$ Ce to $x = 0.8$ Ce indicating that Ce may have reached a solubility limit when $x \geq 0.2$ Ce (described in more detail below). Rietveld refinement of the XRD data was conducted to characterize the effect of Ce doping on the lattice parameter (Table 1). From Table 1, the $x = 0.0$ Ce tetragonal had lattice parameters of $a = b = 13.0682 \text{ \AA}$, $c = 12.70201 \text{ \AA}$, which is in good agreement with similar work $a = b = 13.077 \text{ \AA}$ and $c = 12.715 \text{ \AA}$ [23,25]. Also from Table 1, cubic LLZO lattice parameters are rather independent of the Ce concentration with an average value of 13.065 \AA with a standard deviation of $\pm 0.004 \text{ \AA}$, which is noticeably larger than Ta doped cubic LLZO (12.96 \AA [20,23]) and Nb doped cubic LLZO (12.97 \AA [22]). There have been reports where Ce was used to dope yttrium iron garnet (YIG). A solubility limit of 0.3 mol Ce has been observed in YIG, which is in good agreement with what is observed in this work [26–28]. The work by Sekijima et al. found a continuous increase in the lattice parameter (0.022 \AA) from 0.0 to 0.3 mol Ce in YIG. Additionally, Sekijima et al., confirmed that all of the Ce substituted for Y. In this work, however, there is no noticeable trend between the Ce concentration and the lattice parameter. We believe that Ce may be substituting on both the 24c (La) and 16a (Zr) sites. Upon the initial addition of Ce (0.2 mol), some Ce substitutes on the 24c site to

create Li vacancies and partially stabilize the cubic phase and some Ce substitutes on the 16a site. As the Ce concentration is increased to 0.4 mol, more Ce substitutes on the 24c site expelling enough Li to form fully cubic LLZO while simultaneously doping on the 16a site. However, as more Ce is added, the solubility of Ce on the 24c site reached, but is sufficient to stabilize the cubic phase, and excess Ce may substitute on the 16a site expelling Zr. The presence of Li_2ZrO_3 in the X-ray diffraction patterns when $x > 0.4$ Ce, may explain where the expelled Zr resides (Fig. 1).

Efforts were conducted to investigate the reason behind the relatively significant volume fraction of CeO_2 for all values of $x \geq 0.2$ Ce. Calcining at higher temperatures $> 1000^\circ\text{C}$ was not attempted due to the possibility of increased Li sublimation. Thus, the effect of calcination time, at 1000°C , was explored for one Ce composition ($x = 0.4$ Ce) to determine if more time was needed for Ce to diffuse into the 24c site. The XRD data for $x = 0.4$ Ce calcined at 1000°C for 1, 4 and 24 h are shown in Fig. 2. From Fig. 2, the following observation can be made. The relative fraction of LLZO is significantly reduced when comparing the 4 h calcination to the 24 h calcination. This relative reduction in LLZO is accompanied by the formation of $\text{La}_2\text{Zr}_2\text{O}_7$ as a major phase in the XRD pattern. Although the $\{1\bar{1}1\}$ primary of CeO_2 ($2\theta = 28.54^\circ$) and $\{2\bar{2}2\}$ of $\text{La}_2\text{Zr}_2\text{O}_7$ ($2\theta = 28.662^\circ$) are nearly identical, the inset in Fig. 2 shows that the $\text{La}_2\text{Zr}_2\text{O}_7$ is the most prevalent phase. These data suggest that the formation of $\text{La}_2\text{Zr}_2\text{O}_7$ after 24 h of calcination is a result of Li loss from LLZO. A similar decomposition mechanism was observed by Huang et al. [29]. The results of this study also indicate that the amount of CeO_2 decreased from 6.6 to 4.3 volume percent when the calcination time was extended from 1 to 4 h, respectively. Similarly, the concentration of Ce in the LLZO lattice determined by EDS increased from 0.31 ± 0.04 to 0.34 ± 0.02 mol from 1 to 4 h, respectively. However, when the calcination time was increased to 24 h, there was likely significant Li loss and approximately 49% of the volume was decomposed into $\text{La}_2\text{Zr}_2\text{O}_7$ and CeO_2 . Additionally, the remaining LLZO had lost 0.20 mol Ce (0.18 mol Ce remained in the LLZO lattice) and transformed into the tetragonal phase. Thus, it was shown that of the calcination times studied, the 4 h calcination time resulted in the highest Ce content in the LLZO lattice.

From the above results, it is clear that the substitution of Ce for La results in the stabilization of cubic LLZO when $x \geq 0.2$ mol of Ce substitutes for La according to Equation (5). This confirms the hypothesis that the substitution of a super-valent cation (Ce 4+) for La (3+) creates Li vacancies to stabilize cubic LLZO. Moreover, the critical concentration of Li vacancies necessary to stabilize cubic LLZO (≥ 0.2 mol Ce) is in good agreement with related work involving intentionally added super-valent cations (Table 2). Thus, based on this report and reports from others, we believe that a minimum of between 0.125 and 0.25 mol of Li vacancies is required to stabilize cubic LLZO. More theoretical calculations and experimental verifications are necessary to confirm this.

Table 1
Material properties of the Ce doped samples and dopant free LLZO samples.

Sample	Primary phase	Impurity phase	Lattice constant (\AA)	Relative density (%)	Total conductivity (S cm^{-1})
$x = 0.0$ Ce LLZO	Tetragonal	$\text{La}_2\text{Zr}_2\text{O}_7$	$a = b = 13.068$, $c = 12.702$	95	5.77×10^{-6}
$x = 0.2$ Ce LLZO	Cubic + tetragonal	CeO_2	13.011	—	—
$x = 0.4$ Ce LLZO	Cubic	CeO_2	13.020	96	1.44×10^{-5}
$x = 0.6$ Ce LLZO	Cubic	CeO_2	13.014	96	1.26×10^{-5}
$x = 0.8$ Ce LLZO	Cubic	CeO_2	13.020	—	—

3.2. Microstructural analysis of hot pressed samples

Several formulations were hot pressed for further microstructural and electrochemical analysis. The hot pressed specimens consisted of powders that were pre-calced at 1000°C for 4 h. The formulations were based on $\text{Li}_{7-x}\text{La}_{3-x}\text{Ce}_x\text{Zr}_2\text{O}_{12}$ where $x = 0.0, 0.4$ and 0.6 Ce. The $x = 0.2$ formulation was excluded, because XRD data indicated the presence of mixed tetragonal and cubic phases that would make the microstructural and electrochemical analyses too complex. The $x = 0.8$ Ce formulation was excluded, because the volume fraction of CeO_2 inclusions was considered too high to result in meaningful data.

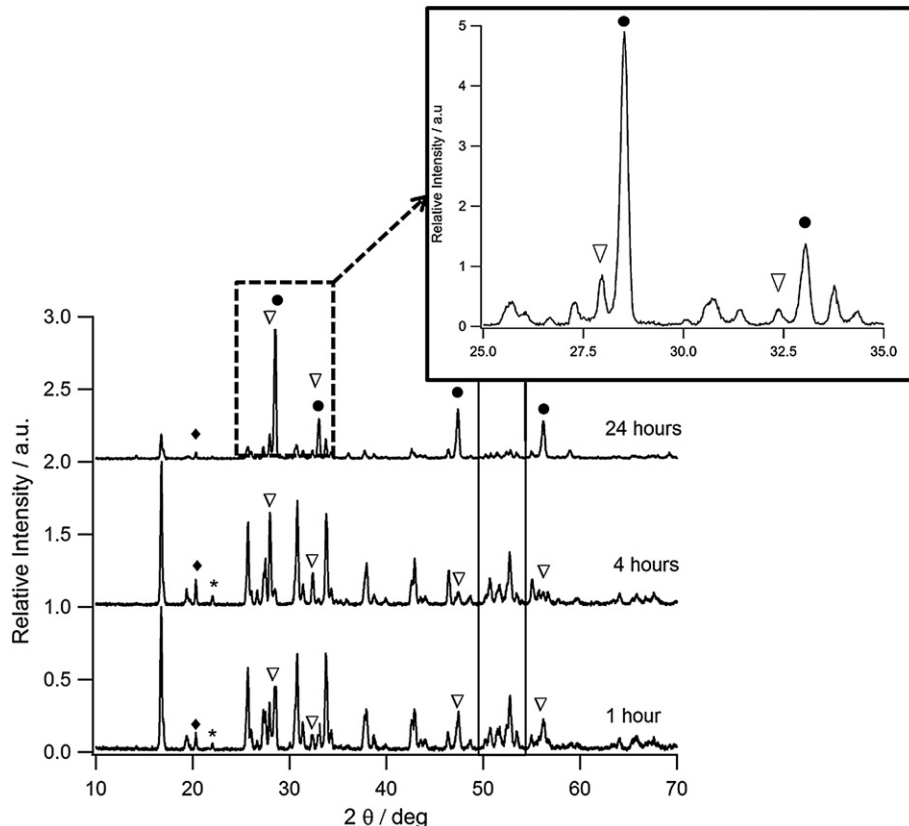


Fig. 2. XRD data for $x = 0.4$ Ce calcined at 1000°C for different durations. ∇ Indicates the presence of CeO_2 ● indicates the presence of $\text{La}_2\text{Zr}_2\text{O}_7$ ◆ indicates the presence of Li_2ZrO_3 and * indicates an unknown phase. The inset for the 24 h calcination sample highlights the presence of CeO_2 along with the $\text{La}_2\text{Zr}_2\text{O}_7$ phase.

Hot pressing at 1000°C resulted in high relative densities ($>94\%$ of the theoretical density) as indicated in Table 1. A typical SEM micrograph of the fractured surface for the $x = 0.4$ Ce specimen is shown in Fig. 3. Fracture surface analysis was also conducted on the other hot pressed samples. There was no significant difference between specimens. Thus, only the $x = 0.4$ Ce specimen is shown for brevity. From Fig. 2, several important points are noted. First, the grain sizes of the $x = 0.4$ Ce specimens were $3\ \mu\text{m}$, which is comparable to the $x = 0$ and 0.6 Ce samples as well as what has been reported in previous work involving Al doping [19]. Second, there appears to be a mixture of inter and intra granular fracture in both Ce doped specimens. Intra granular fracture is evidence of relatively strong bonding between grains, which is likely a result of hot pressing.

Table 2

Summary table of intentionally-added, super-valent cation dopants to stabilize cubic LLZO.

Dopant	Substituted cation	Cubic stabilization concentration (mol)	Total conductivity (S cm^{-1})	Activation energy (eV)
[30] Al ³⁺	Li ⁺	0.23	5.7×10^{-4}	0.35
[18] Al ^{3+,a}	Li ⁺	0.41	2.0×10^{-4}	NR
[19] Al ³⁺	Li ⁺	0.20	4.0×10^{-4}	0.26
[21] Ga ³⁺	Li ⁺	0.25	3.5×10^{-4}	NR
[22] Nb ⁵⁺	Zr ⁴⁺	0.25	NR	NR
[20] Ta ⁵⁺	Zr ⁴⁺	0.25	8.7×10^{-4}	0.22
[22] Ta ⁵⁺	Zr ⁴⁺	0.25	NR	NR
[23] Ta ⁵⁺	Zr ⁴⁺	0.125	NR	NR

NR: Not reported.

^a Microstructural analysis indicated that Al was also present in secondary phases, thus the actual Al concentration in the LLZO lattice was likely lower than 0.41 mol.

Fig. 4 shows the polished, backscattered emission (BSE) image for the $x = 0.4$ Ce specimen (as was the case in the fracture surface analysis, only the $x = 0.4$ Ce specimen is shown for brevity). In the line scan, it is evident that there is a significant increase in Ce and a subtle increase in O as the line crosses over the brighter regions. The BSE analysis indicated that the Ce:O ratio was 1:2, thus confirming that the brighter regions are CeO_2 and are agreement with the XRD data in Fig. 1. The volume fraction of CeO_2 precipitates for $x = 0.4$ Ce and $x = 0.6$ Ce was determined to be 4 and 16%, respectively, confirming that the

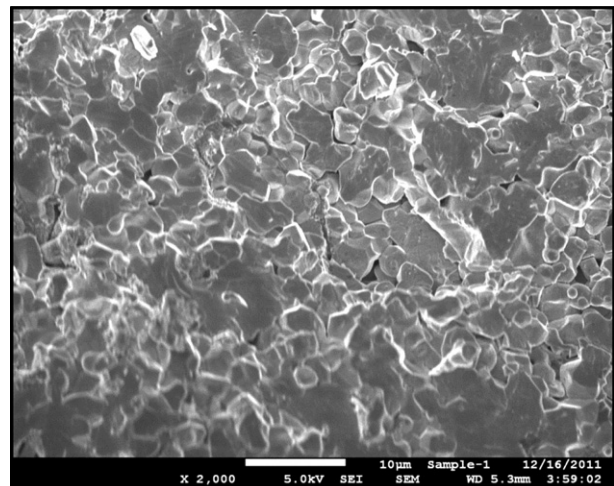


Fig. 3. SEM fracture surfaces for hot pressed $\text{Li}_{6.6}\text{La}_{2.6}\text{Ce}_{0.4}\text{Zr}_2\text{O}_{12}$.

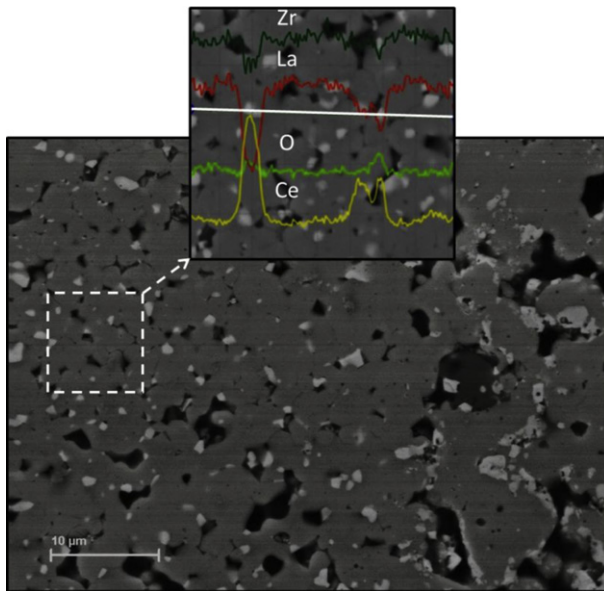


Fig. 4. Backscattered electron micrograph of the polished $x = 0.4$ Ce specimen. The inset shows the EDS line scan.

increased Ce concentration results in excess CeO_2 for the same calcination time (4 h calcination). The BSE images are consistent with the XRD data in Fig. 1 that indicate the presence of CeO_2 and cubic LLZO in the $x = 0.4$ and $x = 0.6$ Ce specimens. Additionally, EDS analysis indicates that Ce concentrations of the $x = 0.4$ and 0.6 Ce specimens had 0.34 and 0.38 mol, respectively, within the LLZO lattice (Table 2). This is in agreement with the data in Fig. 1 that indicate a transition from tetragonal to cubic LLZO above $x \geq 0.2$ Ce.

3.3. Conductivity of Ce doped LLZO

The ionic conductivity was characterized for the hot pressed $x = 0.0, 0.4$ and 0.6 Ce specimens (Fig. 5 and Table 1). The equivalent circuit utilized to obtain the ionic conductivities is included as an inset in Fig. 5. From Fig. 5 and Table 1, several observations can be made. First, the addition of Ce clearly increases the total conductivity compared to the tetragonal ($x = 0.0$ Ce) LLZO. Both of the Ce-

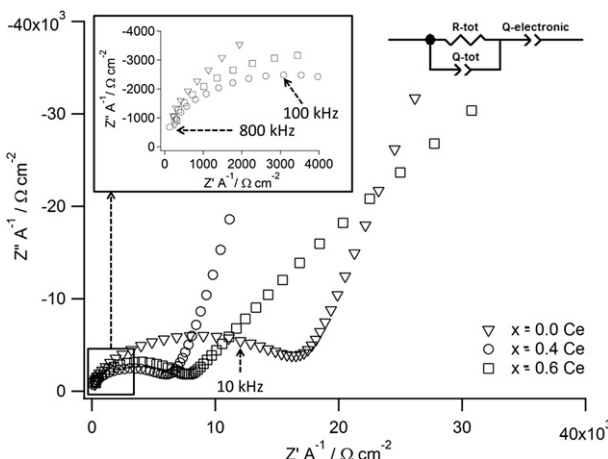


Fig. 5. Nyquist plots for the hot pressed specimens where: $x = 0.0, x = 0.4$ and $x = 0.6$ Ce in the formula: $\text{Li}_{7-x}\text{La}_{3-x}\text{Ce}_x\text{Zr}_2\text{O}_{12}$. The inset highlights the high frequency intercept. The equivalent circuit utilized for obtaining the conductivities is also included.

doped cubic LLZO specimens had more than twice the total conductivity compared to the un-doped tetragonal LLZO (Table 1). However, in comparison to other cubic LLZO samples (Table 2), the Ce-doped specimens had between 15 and 70 times lower total conductivity.

For example, hot pressed Al-stabilized cubic LLZO [19] had a total conductivity of $4.0 \times 10^{-4} \text{ S cm}^{-1}$, which is approximately 30 times higher compared to Ce-stabilized cubic LLZO. Similarly, hot pressed Ta-stabilized cubic LLZO had a total conductivity of $8.7 \times 10^{-4} \text{ S cm}^{-1}$, which is approximately 70 times higher than Ce-stabilized cubic LLZO [20].

Despite the fact that Ce can stabilize the more conductive cubic LLZO phase, it is clear that the total conductivity is considerably lower compared to total conductivity of Al [19] and Ta [20] stabilized cubic LLZO that were also hot pressed with comparable grain sizes and densities. It is important to note, however, that total conductivity (in the Al and Ta doped samples discussed immediately above) was believed to be comparable to the lattice conductivity, because the grain boundary resistance was negligible. We believe that the presence of CeO_2 at the grain boundaries (as evidenced in XRD and BSE analyses) significantly increases the grain boundary resistance, thus resulting in lower total conductivity compared to Al and Ta doped previous work [19,20]. X-ray diffraction data (Fig. 1) indicates that the volume fractions of $\text{La}_2\text{Zr}_2\text{O}_7$ and $\text{Li}_2\text{Zr}_2\text{O}_3$ are minor. Additionally, the conductivity of $\text{La}_2\text{Zr}_2\text{O}_7$ and $\text{Li}_2\text{Zr}_2\text{O}_3$ are likely significantly lower compared to LLZO. The individual contributions of these phases to the total ionic conductivity are, therefore, likely to be insignificant compared to the LLZO majority phase. Also, upon examination of the Nyquist plots, only one semicircular component can be observed. This suggests the presence of only one resistive element in the equivalent circuit. Hence the authors use only a total resistive element (R_{tot}) in the equivalent circuit that factors in the individual contributions of R_{bulk} , $R_{\text{grain boundary}}$, $R_{\text{cerium oxide}}$, $R_{\text{lanthanum zirconium oxide}}$ and $R_{\text{lithium zirconium oxide}}$. As a result, the individual contributions could not be separated over the measured frequency range.

Secondly, the conductivity of the $x = 0.4$ Ce ($1.44 \times 10^{-5} \text{ S cm}^{-1}$) specimen is slightly higher compared to the conductivity of the $x = 0.6$ Ce ($1.26 \times 10^{-5} \text{ S cm}^{-1}$) specimen. Although the $x = 0.4$ Ce had less Ce in the LLZO lattice (0.34 Ce) compared to the $x = 0.6$ Ce (0.38 Ce), any difference in the lattice conductivity is not detectable, again, due to the high grain boundary resistance. We believe that the $x = 0.4$ Ce specimen has a higher total conductivity compared to

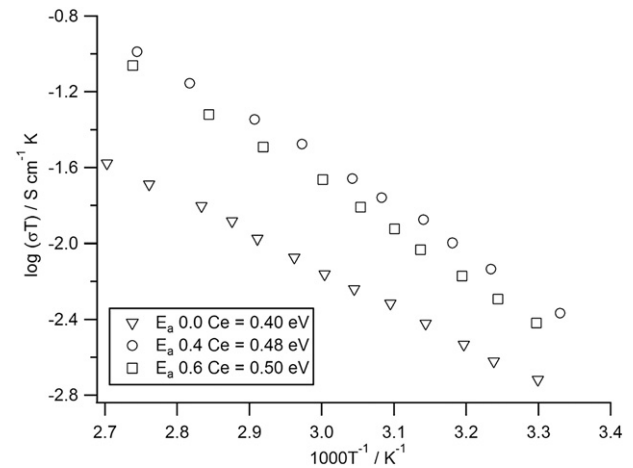


Fig. 6. Arrhenius data for the hot pressed specimens with the following compositions where: $x = 0.0, x = 0.4$ and $x = 0.6$ Ce in the formula: $\text{Li}_{7-x}\text{La}_{3-x}\text{Ce}_x\text{Zr}_2\text{O}_{12}$. Measurements were made between 298 K and 373 K.

the $x = 0.6$ Ce specimen, because there is less CeO_2 present to increase the grain boundary resistance.

The temperature dependence data of the total conductivity for the $x = 0.0$, 0.4 and 0.6 Ce samples are plotted in Fig. 6. The activation energies for the total conductivities in the Ce-doped specimens are 0.48 and 0.50 eV for $x = 0.4$ and 0.6 Ce, respectively. Additionally, although the $x = 0.0$ Ce specimen has a lower total conductivity, the activation energy (0.40 eV) is lower than the two Ce-doped specimens. Compared to other reports (Table 2), the Ce-doped specimens have considerably higher total activation energy compared to other cubic LLZO reports that range from 0.22 to 0.35 eV. The presence of CeO_2 at grain boundaries likely causes high grain boundary resistance, thus increasing the total activation energy despite the possibility of lattice conductivities comparable to other cubic LLZO stabilized with Al, Ga, Nb or Ta.

4. Conclusions

This is the first report describing the tetragonal–cubic phase transition based on Ce (4+) substitution of 24c-La (3+) site in garnet-based electrolytes with the nominal formulation: $\text{Li}_7\text{La}_3\text{Zr}_2\text{O}_{12}$. The higher conductivity cubic LLZO phase was stabilized when $x \geq 0.2$ Ce in $\text{Li}_{7-x}\text{La}_{3-x}\text{Ce}_x\text{Zr}_2\text{O}_{12}$. These data support the hypothesis that super-valent cation doping is what stabilizes cubic LLZO and that the critical concentration of Li vacancies necessary to do so is in the 0.125 – 0.25 mol range. In hot pressed pellets it was determined that Ce-stabilized cubic LLZO has lower total conductivity compared to Al, Ga, Nb and Ta-stabilized (no unintentional Al present) cubic LLZO as a result of the limited solubility of Ce resulting in CeO_2 precipitates, which increase the grain boundary resistance.

Acknowledgements

Authors EL and JS would like to acknowledge the support of the U.S. Army Research Office (ARO). JW and JA would like to acknowledge support of the U. S. Army Research Laboratory (ARL).

References

- [1] Z. Chen, D.J. Lee, Y.K. Sun, K. Amine, MRS Bull. 36 (2011) 498–505.
- [2] P. Balakrishnan, R. Ramesh, T. Premkumar, J. Power Sources 155 (2006) 401–414.
- [3] P. Knauf, Solid State Ion. 180 (2009) 911–916.
- [4] M. Wakihara, T. Minami, M. Tsumisago, C. Iwakura, S. Kohjiya, I. Tanaka, Solid State Ionics for Batteries, Springer, 2005.
- [5] S. Stramare, V. Thangadurai, W. Weppner, Chem. Mater. 15 (2003) 3974–3990.
- [6] Y. Inaguma, C. Liquan, M. Itoh, T. Nakamura, Solid State Commun. 86 (1993) 689–693.
- [7] O. Bohnke, Solid State Ion. 179 (2008) 9–15.
- [8] H. Nakano, K. Dokko, M. Hara, Y. Isshiki, K. Kanamura, Ionics 14 (2007) 173–177.
- [9] M. Hara, H. Nakano, K. Dokko, S. Okuda, A. Kaeriyama, K. Kanamura, J. Power Sources 189 (2009) 485–489.
- [10] R. Murugan, V. Thangadurai, W. Weppner, Angew. Chem. Int. Ed. 46 (2007) 7778–7781.
- [11] M. Kotobuki, H. Munakata, K. Kanamura, Y. Sato, T. Yoshida, J. Electrochem. Soc. 157 (2010) A1076–A1079.
- [12] S. Ohta, T. Kobayashi, T. Asaoaka, J. Power Sources 196 (2011) 3342–3345.
- [13] J. Awaka, N. Kijima, H. Hayakawa, J. Akimoto, J. Solid State Chem. 182 (2009) 2046–2052.
- [14] S. Kumazaki, Y. Iriyama, K.H. Kim, R. Murugan, K. Tanabe, K. Yamamoto, T.T. Hirayama, Z. Ogumi, Electrochim. Commun. 13 (2011) 509–512.
- [15] I. Kokal, M. Somer, P.H.L. Notten, H.T. Hintzen, Solid State Ion. 185 (2011) 42–46.
- [16] E.A. Il'ina, O.L. Andreev, B.D. Antonov, N.N. Batalov, J. Power Sources 201 (2012) 169–173.
- [17] C.A. Geiger, E. Alekseev, B. Lazic, M. Fisch, T. Armbruster, R. Langner, M. Fechtelkord, N. Kim, T. Pettke, W. Weppner, Inorg. Chem. 50 (2010) 1089–1097.
- [18] Y. Jin, P.J. McGinn, J. Power Sources 196 (2011) 8683–8687.
- [19] E. Rangasamy, J. Wolfenstine, J. Sakamoto, Solid State Ion. 206 (2012) 28–32.
- [20] J.L. Allen, J. Wolfenstine, E. Rangasamy, J. Sakamoto, J. Power Sources 206 (2012) 315–319.
- [21] J. Wolfenstine, J. Ratchford, E. Rangasamy, J. Sakamoto, J.L. Allen, Mater. Chem. Phys. 134 (2012) 571–575.
- [22] S. Adams, R.P. Rao, J. Mater. Chem. 22 (2012) 1426.
- [23] A. Logéat, T. Köhler, U. Eisele, B. Stiasny, A. Harzer, M. Tovar, A. Senyshyn, H. Ehrenberg, B. Kozinsky, Solid State Ion. 206 (2012) 33–38.
- [24] M. Barsoum, Fundamentals of Ceramics (Series in Material Science and Engineering), Taylor & Francis, 2002.
- [25] J. Wolfenstine, E. Rangasamy, J.L. Allen, J. Sakamoto, J. Power Sources 208 (2012) 193–196.
- [26] T. Sekijima, H. Itoh, T. Fujii, K. Wakino, M. Okada, J. Cryst. Growth 229 (2001) 409–414.
- [27] N.B. Ibrahim, C. Edwards, S.B. Palmer, J. Magn. Magn. Mater. 220 (2000) 183–194.
- [28] T.C. Mao, J.C. Chen, J. Magn. Magn. Mater. 302 (2006) 74–81.
- [29] M. Huang, T. Liu, Y. Deng, H. Geng, Y. Shen, Y. Lin, C.W. Nan, Solid State Ion. 204–205 (2011) 41–45.
- [30] Y. Shimonishi, A. Toda, T. Zhang, A. Hirano, N. Imanishi, O. Yamamoto, Y. Takeda, Solid State Ion. 183 (2011) 48–53.